Carotid artery wall segmentation in multispectral MRI by coupled optimal surface graph cuts

Arias-Lorza, Andrés M.; Petersen, Jens; van Engelen, Arna; Selwaness, Mariana; van der Lugt, Aad; J. Niessen, Wiro; de Bruijne, Marleen

Published in:
IEEE Transactions on Medical Imaging

DOI:
10.1109/TMI.2015.2501751

Publication date:
2016

Document version
Peer reviewed version

Carotid Artery Wall Segmentation in Multispectral MRI by Coupled Optimal Surface Graph Cuts

Andrés M. Arias-Lorza[1], Jens Petersen[2], Arna van Engelen[1], Mariana Selwaness[3,4], Aad van der Lugt[4], Wiro J. Niessen[1,5], and Marleen de Bruijne [1,2]

***Abstract*—We present a new three-dimensional coupled optimal surface graph-cut algorithm to segment the wall of the carotid artery bifurcation from Magnetic Resonance (MR) images. The method combines the search for both inner and outer borders into a single graph cut and uses cost functions that integrate information from multiple sequences. Our approach requires manual localization of only three seed points indicating the start and end points of the segmentation in the internal, external, and common carotid artery. We performed a quantitative validation using images of 57 carotid arteries. Dice overlap of 0.86 ± 0.06 for the complete vessel and 0.89 ± 0.05 for the lumen compared to manual annotation were obtained. Reproducibility tests were performed in 60 scans acquired with an interval of 15 ± 9 days, showing good agreement between baseline and follow-up segmentations with intraclass correlations of 0.96 and 0.74 for the lumen and complete vessel volumes respectively.**

***Index Terms*—Carotid artery, Magnetic resonance imaging (MRI), Optimal surface graph, Wall segmentation.**

I. Introduction

Atherosclerosis is one of the primary causes of death in the world [1]. Atherosclerotic plaques in the carotid arteries may rupture causing thrombus formation and embolization of plaque content and/or thrombus into the distal intracranial vessel resulting in a stroke [2]. For risk assessment, detection of plaque and accurate quantification of plaque volume is important.

Magnetic Resonance (MR) enables 3D imaging of the carotid artery vessel wall [3], [4]. For a proper analysis of the vessel wall, segmentation of both vessel lumen and outer vessel wall is required. Manual segmentation of the vessel walls in MR images is a time consuming process and subject to inter-observer variability [5]. Therefore, automatic techniques for segmenting the vessel wall are highly desirable.

Several automatic and semi-automatic methods have been proposed to segment the artery wall in MR images [6], [7], [8], [9], [10], [11], [12]. The methods presented in [6], [7], [8] are based on deformable models and can only segment the inner border. [9], [10], [11], [12] are able to segment inner and outer artery walls. Van 't Klooster et al. [9] proposed a 3D deformable vessel model, in which a vessel is modeled using a cylindrical surface that can be modified by moving control points located on the model surface. Good results were reported on Proton Density Weighted (PDw) Black-Blood MRI (BBMRI) images. However, only the Common Carotid Artery (CCA) and not the bifurcation region were segmented. This method also uses a local optimization procedure with the lumen segmentation as initialization, which may get stuck in a local optimum for instance in diseased vessels where the distance between the inner and outer wall is large. Hameeteman et al. [12] extended this method with a learning-based postprocessing step. In this approach, two separate cylindrical deformable surface models must be used to segment from CCA to the Internal Carotid Artery (ICA), and from CCA to the External Carotid Artery (ECA), which may lead to inaccuracies in the bifurcation area. Recently, Ukwatta et al. [10] proposed a globally optimal evolution approach for segmenting the carotid artery wall from BBMRI images. They obtained good results segmenting the complete bifurcation region with low processing times. This method requires the initial estimation of the intensity probability density functions of the lumen, wall, and background using marks of the three regions on a 2D transverse slice. Therefore, problems may arise at sections of the artery that are different from the estimated probability density functions.

Graph-based methods have been used for segmenting various types of vessels on several imaging modalities obtaining promising results [11], [13], [14], [15], [16]. Most common are voxel-based graph cut methods which represent the voxels of an image as vertices in a graph. Generally, in these approaches all vertices are connected to the sink and source vertices, and only neighbor vertices are linked. This approach allows cuts between neighboring voxels to segment foreground and background regions. A fully automatic voxel-based graph method to segment the aortic arch and carotid artery from CTA scans was proposed by Freiman et al. [13]. Bauer et al. [14] proposed another voxel-based graph method to segment vessels, in which an energy function that combines gradient magnitude information and the distance to an initialization shape is minimized.

A second class of graph-based methods is the optimal surface methods [11], [15], [17], [18], [19]. Here the graph vertices represent image positions, and these are arranged in

This research was financially supported by the Netherlands Organization for Scientific Research (NWO).

Contact e-mail: a.ariaslorza@erasmusmc.nl

[1]Biomedical Imaging Group Rotterdam, Departments of Radiology and Medical Informatics, Erasmus MC, Rotterdam, The Netherlands.

[2]Image Section, Department of Computer Science, University of Copenhagen, Denmark.

[3]Department of Biomedical Engineering, Erasmus MC, Rotterdam, The Netherlands.

[4]Department of Radiology, Erasmus MC, Rotterdam, The Netherlands.

[5]Faculty of Applied Sciences, Department of Imaging Science and Technology, Delft University of Technology, The Netherlands.

columns. Each of these columns intersects the sought surface, and the positions where the columns intersect the surface discretely represent the segmentation solution. This construction makes it possible to enforce topology constraints and to incorporate an initialization volume in the graph structure. Often, the graph is defined based on a coarse initial segmentation. Petersen et al. [18] proposed to generate the graph columns from an initial segmentation surface using non-intersecting columns based on flow lines and applied this to segment airways in CT images. These non-intersecting columns avoid self-intersecting surface results, making it possible to segment high curvature surfaces such as the bifurcation of airways or vessels. In a preliminary study of the present work, we adapted this approach to segment the carotid artery wall on individual MRI sequences [11]. However, if the image information of the individual MRI sequences is combined and integrated into a surface graph, it may provide more accurate border locations since different image sequences have better contrast either at the inner or outer wall.

In this paper, we present an extension of this previous work [11] which uses an optimal surface graph to segment the complete carotid artery wall bifurcation on MRI images using minimal user interaction. This method guarantees global minimization of a cost function, ensuring smooth surfaces and topological constraints between surfaces. The contributions of this paper are as follows:

- New graph edge cost function that integrates information from several images.
- Initialization using an automated centerline extraction method as opposed to [11] which requires a lumen segmentation.
- A much extended validation compared to [11]: 57 carotid arteries in contrast to 32, parameter optimization and evaluation by full data set evaluation using a cross-validation approach in contrast to data set division, many more manually annotated cross-sections (one for every 1mm centerline in contrast to 6 cross-sections per artery at random positions).
- We present improved results compared to [11]. Additionally, we extended the evaluation including inter-observer variability analysis, scan-rescan reproducibility test, and comparison with a state-of-the-art MRI artery wall segmentation method [12] on a public database.

II. Method

A. Method overview

The main steps of the method are:

1) Obtain a 3D coarse segmentation of the lumen as initialization. This segmentation is obtained by a dilation of an extracted artery centerline.
2) Based on the initialization construct the surface graph. The steps to construct the graph are:
   a) Obtain from the initialization the graph column trajectories.
   b) On the graph column trajectories assign the graph vertices.
   c) Assign graph edges between vertices with a respective cost. The cost for edges between graph columns is given by a constant value, while the cost of the edges in a column is a function of the image information.
3) Compute minimum graph cut. The segmented surface is located at the cut locations.

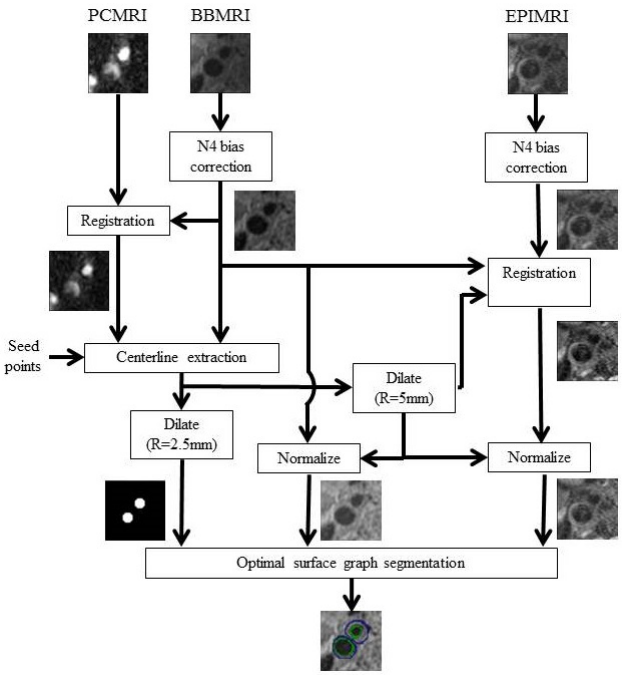

Fig. 1. Schematic of the segmentation method. At the top the used images are shown, next are depicted the preprocessing steps. Finally, at the bottom the segmentation is shown using the proposed method.

B. Initialization by centerline extraction

To build the graph we require a coarse initial segmentation. From this initial segmentation the graph columns are constructed. The coarse initial segmentation is obtained by computing the centerline of the vessel lumen using the semi-automatic centerline extraction method proposed by Tang et al. [6]. In this method, the lumen centerline is determined as the minimum cost path between user-defined seed points in the common $\boldsymbol{x}_c$, internal $\boldsymbol{x}_i$, and external $\boldsymbol{x}_e$ carotid arteries. Two minimum cost paths are computed, one between $\boldsymbol{x}_c$ and $\boldsymbol{x}_i$ (we denote the set of points that define this path by $\boldsymbol{C}^i$), and the other between $\boldsymbol{x}_c$ and $\boldsymbol{x}_e$ ($\boldsymbol{C}^e$). The cost is defined by a combination of the inverse of medialness filtering [20] and inverse of lumen intensity similarity metric [6] outputs. The minimum cost path is obtained by applying Dijkstra's algorithm. Subsequently, the centerline is refined by re-computing the minimum cost path after multi-planar reformatting perpendicular to the centerline [6]. The two obtained centerlines $\boldsymbol{C}^i$ and $\boldsymbol{C}^e$ are connected in order to have the centerline of the complete artery: $\boldsymbol{C} = \boldsymbol{C}^i \cup \boldsymbol{C}^e$. Finally, we obtain a 3D binary image representation of the centerlines I^c: $\mathbb{Z}^3 \rightarrow \{0, 1\}$ by mapping the centerline set of image positions $\boldsymbol{C}$ to a binary scalar space I^c.

A coarse approximation of the lumen Q: $\mathbb{Z}^3 \rightarrow \{0,1\}$ is obtained by computing a binary morphological dilation of I^c with a disk structuring element with radius R.

C. Optimal surface graph construction and optimization

Based on the coarse initial segmentation Q, we construct the graph $G = (V, E)$ with vertices V and edges E. The vertices are associated with positions in the image, and represent potential border locations. As in [18], these are grouped by non-intersecting graph columns, which guarantee non self-intersecting segmentations. The set of edges E connects the vertices of the graph, and represents the association between vertices. High-cost edges are expected to connect vertices of the same class. Low-cost edges are expected between vertices from different classes. The segmentation solution is given by the minimum graph cut, which represents the separation of the graph vertices in two sets: source part $V_s \subseteq V$ (foreground) and sink part $V_t \subseteq V$ (background), such that $V_t = V \backslash V_s$. In our case we have two surfaces to segment, the inner and the outer carotid artery wall, therefore coupling two graphs is necessary to find both borders simultaneously. One graph is used to separate the vessel lumen from the wall and background while the other graph is used to separate the lumen and wall from the background. We represent the coupling of graphs by connecting vertices of the two sub-graphs. This graph construction approach coupling several graphs is described in detail in section II-C2. A minimal cut minimizes the total cost of the edges that are being cut [21]:

$$\begin{aligned} &\min_{v_i \in V_s,\ v_j \in V_t} \sum Cost(v_i \rightarrow v_j), \\ &s.t. \quad s \in V_s, t \in V_t, V_t = V \backslash V_s, (v_i \rightarrow v_j) \in E, \end{aligned} \tag{1}$$

where $Cost(v_i \rightarrow v_j)$ is the associated cost of the directed edge $v_i \rightarrow v_j$ between the vertices v_i and v_j, and the vertices s and t denote the source and sink points of the graph. This minimization is solved by applying a min-cut/max-flow optimization algorithm [22].

The following three subsections explain in detail the graph construction approach.

1) Graph column trajectories: To construct the graph, first the graph columns have to be traced in the image. Each graph column is composed of a set of vertices representing the possible image positions the surface can take. The graph column trajectories are traced from the surface voxels of the coarse initial segmentation Q. This set of image locations at the starting surface is represented by $\mathbf{X}_Q = \{\boldsymbol{x}_{i,0} | \, i \in \{0, .., N_Q\}\}$, where N_Q is the number of voxels on the surface.

A requirement to guarantee segmented surfaces that do not self-intersect is that the graph columns do not intersect each other [18]. Graph columns based on flow lines as described in [18] have these characteristics. Here, the graph columns are traced from $\boldsymbol{x}_{i,0}$, and follow the flow lines $\boldsymbol{f}_i$: $\mathbb{R} \rightarrow \mathbb{R}^3$ of the gradient vector field of a Gaussian smoothing of the initial segmentation represented by Q_σ: $\mathbb{R}^3 \rightarrow \mathbb{R}$, where σ^2 represents the variance of the Gaussian kernel. That is, the flow lines $\boldsymbol{f}_i$ are obtained by solving:

$$\frac{\partial \boldsymbol{f}_i}{\partial t}(t) = \nabla Q_\sigma(\boldsymbol{f}_i(t)), \tag{2}$$

with initial value given by $\boldsymbol{f}_i(0) = \boldsymbol{x}_{i,0}$. These flow lines vary in length depending on the point where the gradient of the scalar field Q_σ flattens. A schematic of a gradient vector field of a smoothed segmentation Q_σ is shown in Fig. 2(a). A 2D sketch of the flow lines traced along this gradient vector field, starting from the graph vertices located at the initialization surface is depicted in Fig. 2(b).

2) Graph construction:

a) Graph vertices: Solving Eq. 2 for all $\boldsymbol{x}_{i,0} \in \mathbf{X}_Q$ such that $\boldsymbol{f}_i(0) = \boldsymbol{x}_{i,0}$ leads to all graph columns. Each individual flow line $\boldsymbol{f}_i$ defines two graph columns: V_i^{Inner} and V_i^{Outer}, whose vertices represent sets of possible positions for the inner and the outer wall respectively.

Using the Runge-Kutta-Fehlberg method, the solution of $\boldsymbol{f}_i(t)$ in Eq. 2 is approximated at regular intervals δ defining the positions of the graph vertices by:

$$\boldsymbol{x}_{i,k} = \boldsymbol{f}_i(k\delta), \tag{3}$$

where $k \in \mathbb{Z}$, $\boldsymbol{x}_{i,k}$ is the image position associated with the graph vertex $v_{i,k}^m$. For each vertex $v_{i,k}^m$, $m \in M$ and $M = \{Inner, Outer\}$ represent the set of surfaces to find. The vertex $v_{i,k}^m$ is part of the graph column V_i^m, such that $V_i^m = \left\{ v_{i,k}^m \middle| \, k = -I_i, I_i + 1, \ldots, 0, \ldots, O_i - 1, O_i \right\}$, where the vertices $v_{i,0}^m$ represent positions at the initial surface given by $\boldsymbol{x}_{i,0}$, and $v_{i,-I_i}^m$ and v_{i,O_i}^m represent the innermost and outermost vertices of column V_i^m. Each vertex $v_{i,k}^m$ describes a possible position of wall m in column V_i^m. An example depicting this graph column construction based on flow lines is shown in Fig. 2(c).

The complete set of vertices of the graph is represented by the set of all column vertices and the vertices s and t. Unlike the vertices of a column V_i^m, s and t do not have an associated position in the image. Thus the complete set of vertices V is defined by:

$$\begin{aligned} &V = \left\{ \bigcup_{i,m} V_i^m \right\} \cup \{s, t\}, \\ &s.t. \quad i \in \{0, .., N_Q\}, M = \{Inner, Outer\}. \end{aligned} \tag{4}$$

b) Graph edges: The set of edges E connects the vertices of the graph, and represents the association between vertices. The edge between the vertices $v_{i,k_1}^{m_1}$ and $v_{j,k_2}^{m_2}$ is denoted by $v_{i,k_1}^{m_1} \rightarrow v_{j,k_2}^{m_2}$ with an associated cost of $Cost(v_{i,k_1}^{m_1} \rightarrow v_{j,k_2}^{m_2})$.

The edge set E consists of intra-column edges E_{intra} and inter-column edges E_{inter} [11], [18].

- **Intra-column edges:** The intra-column edges E_{intra} connect two consecutive vertices $v_{i,k}^m$ and $v_{i,k+1}^m$ in the same column by directed edges. The cost of edges $v_{i,k}^m \rightarrow v_{i,k+1}^m$ represents local image information associated with the border location, and must satisfy the condition $Cost(v_{i,k}^m \rightarrow v_{i,k+1}^m) \geq 0$ [18]. To ensure the surfaces cross each column only once, the edges $v_{i,k+1}^m \rightarrow v_{i,k}^m$ are assigned an infinite cost. Finally, the source vertex s is connected to all innermost vertices

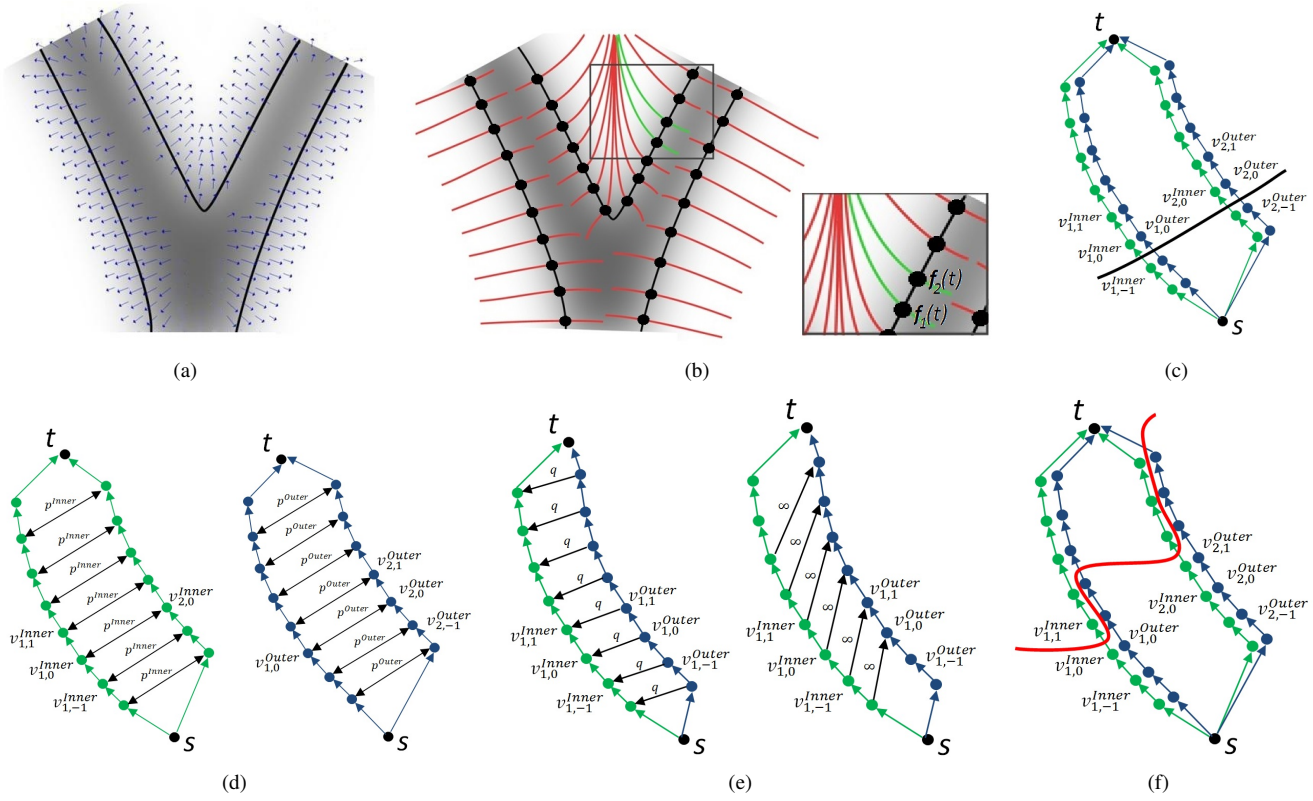

Fig. 2. Construction of graph columns based on flow lines. First, the coarse initial segmentation is smoothed (gray colored tubular structure) and a gradient vector field is computed, see (a). Subsequently, (b) shows the flow lines represented by red lines which trace this gradient field both inwards and outwards from the initialization surface vertices represented by dots. These flow lines represent the graph columns trajectories. Two flow lines $\boldsymbol{f}_1(t)$ and $\boldsymbol{f}_2(t)$ indicated by the green curves are selected. In (c), each of these two flow lines represent two graph columns: inner (green dots) and outer (blue dots) wall columns. The graph column vertices are indicated by the dots. Here, some of the vertices labels are shown. The intra-column edges are depicted by arrows. The black dots *s* and *t* are the source and sink vertices respectively, and the initialization surface is represented by the black curve. Further, the smooth penalty edges are shown in (d) and the surface coupling edges in (e). Finally, a graph cut example represented by a red curve is depicted in (f).

in the graph by $s \overset{\infty}{\rightarrow} v^m_{i,-I_i}$, and all outermost vertices are connected to the sink vertex t by $v^m_{i,O_i} \overset{Cost(v^m_{i,O_i}\rightarrow t)}{\rightarrow} t$. Note: $Cost(v^m_{i,O_i}\rightarrow t)$ is equivalent to $Cost(v^m_{i,O_i}\rightarrow v^m_{i,O_i+1})$, where t represents the nonexisting vertex v^m_{i,O_i+1}. A representation of the intra-column edges is shown in Fig. 2(c).

The intra-column edge cost in column V^m_i should indicate the border location, and therefore the minimum should be at the position of surface m. We achieve a low cost $Cost(v^m_{i,k}\rightarrow v^m_{i,k+1})$ at the image border, by letting the cost be inversely proportional to the first order derivative of the image intensity $\frac{\partial \tilde{I}^{s_q}(\boldsymbol{f}_i(t))}{\partial t}$ along the graph column trajectory $\boldsymbol{f}_i$, where $\tilde{I}^{s_q}(\boldsymbol{f}_i(t))$ is a cubic interpolation of the MRI image sequence s_q: I^{s_q}: $\mathbb{Z}^3 \rightarrow \mathbb{R}$, at the position $\boldsymbol{f}_i(t)$. The MRI image intensity transitions from low to high from the lumen to the vessel wall, and usually from high to low intensity from the vessel wall to the background. Therefore only the positive part of $\frac{\partial \tilde{I}^{s_q}(\boldsymbol{f}_i(t))}{\partial t}$ is considered for $Cost(v^{Inner}_{i,k}\rightarrow v^{Inner}_{i,k+1})$, whereas for $Cost(v^{Outer}_{i,k}\rightarrow v^{Outer}_{i,k+1})$ only the negative part is considered.

Costs obtained from different spatially registered MR sequences are combined in a weighted sum, with the weights for inner and outer surfaces tuned separately. This approach may provide more accurate border locations since different image sequences have better contrast either at the inner or outer wall. Therefore, we define the intra-column cost by the equation:

$$Cost(v^m_{i,k}\rightarrow v^m_{i,k+1}) = K^m - \sum_{s_q\in S} \beta^{m,s_q} \left| \frac{\partial \tilde{I}^{s_q}(\boldsymbol{f}_i(k\delta))}{\partial t} \right|^{Sign(m)}, \quad (5)$$

with $Sign(m) = \begin{cases} + & if\ m = Inner \\ - & if\ m = Outer \end{cases}$, S represents the set of MRI image sequences, and $\beta^{m,s_q} \in [0,1]$ is a weighting parameter that indicates the contribution of each image sequence, such that $\sum_{s_q\in S} \beta^{m,s_q} = 1$. In Eq. 5, K^{Inner} and K^{Outer} represent respectively the most positive and most negative part of the weighted sum of the first order derivatives in the entire graph, such that $Cost(v^m_{i,k}\rightarrow v^m_{i,k+1}) \geq 0$. The derivatives in Eq. 5 are computed using central differences from the interpolated image intensity values along the flow-lines.

-**Inter-column edges:** The edges between columns E_{inter} incorporate information from different graph columns. Using these, the wall position can be determined in graph columns in which the boundaries are not clearly visible. There are two

types of edges: smooth penalty edges, and surface coupling edges.

Smooth penalty edges represented by $v^m_{i,k} \leftrightarrow v^m_{j,k}$ between the neighboring columns V^m_i and V^m_j, penalize irregularities, ensuring smooth segmentations. When the length of two neighboring columns is different, the remaining vertices at the innermost part of the column are connected to the source vertex *s*, and the remaining vertices at the outermost part of the column are connected to the sink *t* [18]. As in [11], we linearly penalize (Eq. 1) displacements of the graph cut between neighboring columns. To do this, the cost of these edges is given by a constant value p^m for each surface *m*: $v^m_{i,k} \overset{p^m}{\longleftrightarrow} v^m_{j,k}$. A representation of the smooth penalty edges is shown in Fig. 2(d).

Surface coupling edges are used to obtain topologically correct segmentations by constraining or penalizing the distance between the inner and outer walls. To ensure that the outer surface is outside the inner surface with a minimum distance of Δ vertices, we assign edges an infinite cost: $v^{Inner}_{i,k} \overset{\infty}{\rightarrow} v^{Outer}_{i,k+\Delta}$; and to linearly penalize the distance between the inner and outer wall, we assign the edges $v^{Inner}_{i,k} \overset{q}{\leftarrow} v^{Outer}_{i,k}$ with a constant cost value *q*. A representation of the surface coupling edges is shown in Fig. 2(e).

III. Experiments and Results

A. Image Data

To validate the proposed method, we used MRI of the carotid bifurcation from 31 subjects with carotid artery plaques with at least one artery with a maximum wall thickness $\geq 2.5\,mm$ measured in ultrasound from the Rotterdam study [23]. Five arteries were excluded due to manual annotation errors. Therefore, 57 carotid arteries were used to evaluate the proposed method. We used both PDw-BBMRI and Phase Contrast MRI (PCMRI) images to compute the lumen centerline [6], which serves as initialization to construct the graph. In addition, we used PDw Echo Planar Imaging MRI (EPIMRI) and/or BBMRI images to compute the intra-column edge cost in Eq. 5. The acquisition time for each sequence is between $\sim$3 min and $\sim$6 min. EPIMRI images clearly distinguish the carotid artery wall [11], while in BBMRI the artery lumen is well defined [24]. In this study we compare segmentation results using either one of the two images (EPIMRI or BBMRI), and the combination of those. The BBMRI images have an in-plane voxel size of 0.507×0.507mm and 0.9mm slice thickness, while the PCMRI images have $0.703 \times 0.703 \times 1$mm, and the EPIMRI images $0.507 \times 0.507 \times 1.2$mm (see Van den Bouwhuijsen et al. [23] for details of the acquisition protocol).

B. Manual annotations

To evaluate and to optimize the parameters of the presented method, we used manual annotations in all BBMRI images. We used a similar manual annotation framework as described for CTA images in [5]. Here, the manual annotation process starts with a manual definition of the centerline. Subsequently, longitudinal contours along this centerline were drawn in a curved planar reformatted image for both the inner and outer border. These longitudinal contours were then used to create cross-sectional contour images at 1mm intervals perpendicular to the centerline. Subsequently, all cross-sectional images were checked and contours were adjusted when needed. The resulting cross-sectional contour images were re-sampled at a resolution of 0.05×0.05mm, so ten times higher than the in-plane original image resolution, which permits validating the proposed method at a higher accuracy. Since the length of the automatic and manual centerlines may differ, cross-sections for which the automatic centerline is not defined are discarded from the evaluation.

For cases where it is not possible to evaluate the cross-sectional contours (Subsection III-D and III-H), we compared 3D masks for the lumen and the complete vessel. These 3D masks were obtained by generating a 3D implicit function from the cross-sectional contours, which subsequently is filled to create the 3D masks [25]. The 3D masks of the lumen are obtained from the inner wall contours and the complete vessel 3D mask from the outer wall contours.

C. Preprocessing

The BBMRI and EPIMRI images suffer from intensity inhomogeneity within the neck area [12]. This was corrected using N4 bias field correction [26], which is one of the most popular methods to correct intensity nonuniformity in MRI data. We used the default parameters of the method on the complete image as described in [26].

To compute the lumen centerline for initialization we followed the same procedure as in [6]. First we registered PCMRI to BBMRI using 3D rigid transformation followed by a 3D affine transformation, with mutual information as similarity metric. Subsequently, three seed points were manually placed by an expert in the BBMRI images and the centerlines were computed using a cost obtained from BBMRI and PCMRI images as described in section II-B.

The graph initializations were obtained by dilating the resulting centerlines using a disk structuring element with radius *R* of 2.5mm. The value of R was selected based on the average radius of the carotid artery which is between 2.3mm and 3.05mm depending on gender and section of the artery [27].

Subsequently, all EPI images were non-rigidly registered to the BBMRI data. We used the registration configuration presented in [28]. Here, a circular registration mask of 10mm diameter which covers the complete vessel was required. We obtained this by dilating the centerlines using a disk structuring element with a radius of 5mm. As suggested in [28], we used a 3D B-spline transformation with 15mm grid spacing, and mutual information as similarity metric.

Finally, we normalized the image intensities by a linear intensity normalization. For each image I^{s_q} with $s_q \in \{BBMRI, EPIMRI\}$, we computed the intensity values that accumulate 5%: $I^{s_q}_{5\%}$, and 95%: $I^{s_q}_{95\%}$ of the intensities distribution inside the same 10mm-diameter circular mask. Subsequently, these intensity values were scaled between 0 and 255 to obtain the normalized image $I^{s_q}_N$ by: $I^{s_q}_N(\mathbf{x}) =$

TABLE I
DETERMINED BEST SET OF PARAMETERS USING EACH IMAGE SEQUENCE AND THE COMBINATION. THESE WERE OBTAINED APPLYING A THREE-FOLD CROSS-VALIDATION AND AN ITERATIVE RANDOM BINARY SEARCH ALGORITHM [18]. REMARK: THE VALUES ARE THE MEANS OBTAINED FROM THE THREE FOLDS, AND BETWEEN BRACKETS THE RANGE IS SHOWN.

Image Sequence	**Best set of Parameters**					
	$\sigma(mm)$	p^{Inner}	p^{Outer}	q	$\beta^{Inner,BBMRI}$	$\beta^{Outer,BBMRI}$
BBMRI	2.25 [2 2.5]	66.3 [43.8 103.9]	573.3 [529.5 625]	0	1	1
EPIMRI	1.7 [1.5 2]	189.6 [127.7 257.8]	548.6 [412.9 700]	0	0	0
BBMRI & EPIMRI	1.63 [0.9 2]	107.81 [92.5 121.87]	387.47 [98.7 550]	0	0.91 [0.75 1]	0.58 [0 0.93]

$255\frac{I^{sq}(\mathbf{x})-I^{sq}_{5\%}}{I^{sq}_{95\%}-I^{sq}_{5\%}}$. These images are used to compute the intra-column cost defined in Eq. 5. A schematic of the preprocessing including the segmentation is shown in Fig. 1.

D. Inter-observer variability

We compared manual annotations performed by two different experts with similar experience to assess inter-observer agreement. ICA and CCA were manually annotated by both observers in a subset of 28 carotid arteries. However, the generated cross-sectional contours for the two observers are at different positions due to differences in the manually annotated centerlines. Therefore, comparing the manually annotated cross-sections was not possible, and instead we generated 3D masks for the lumen and the complete vessel based on the cross-sectional contours of the inner and outer wall. To compare the 3D masks, we axially cropped the volumes such that the masks of both observers were defined on the same axial image slices in the cropped volume. We measured the volume overlap between observers by computing the Dice Similarity Coefficient (DSC) [29]. The obtained average DSC between observers was 0.81 ± 0.04 for the lumen and 0.91 ± 0.04 for the complete vessel. Fig. 3 shows scatter plots describing the correlation of lumen and vessel wall (complete vessel segmentation minus lumen segmentation) volumes between the two observers. The obtained Intraclass Correlation Coefficient (ICC) for the lumen volumes was $ICC = 0.82$, and for the wall $ICC = 0.63$. We performed Friedman analysis, which is a non-parametric statistical test that allows comparing > 2 results at the same time. We found that the volumes from both observers were significantly different for the lumen and for the wall $(p < 0.01)$.

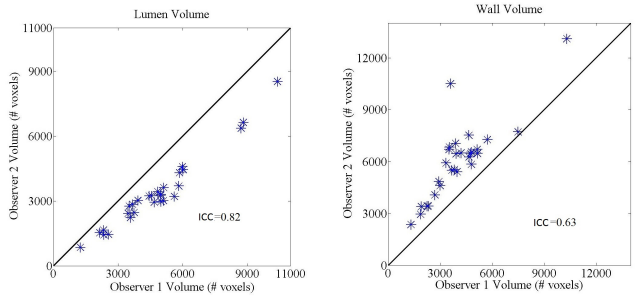

(a) (b)

Fig. 3. Scatter plots comparing observer 1 and observer 2 for segmented lumen volumes (a), and wall volumes (complete vessel minus lumen segmentation) (b), for 28 carotid arteries.

E. Parameter Tuning

Three-fold cross-validation experiments were performed in which the best set of parameters were determined on 20-21 images and subsequently used to segment the held out 10-11 images. This cross-validation allows evaluating the method on the complete data set, and the results represent performance on unseen data acquired with a similar scan protocol. To approximate the best set of parameters, we used an iterative random binary search algorithm [18] to find the parameter set that maximizes the average vessel wall DSC between the automatically and manually segmented cross-sections from observer 1. Based on our previous work [11], we fixed the sampling interval of the flow lines δ described in section II-C2a to 0.35mm. The minimum distance between inner and outer borders in the graph Δ is fixed to two vertices: $\Delta = 2$, which represents a distance of 0.7mm (the minimum carotid wall thickness is about 0.8mm [30]). The parameters to optimize are then: the σ of the Gaussian kernel used to smooth the initial segmentation defined in section II-C1; the smoothness penalties p^{Inner}, p^{Outer}, the inner-outer border separation penalty q defined in section II-C2b; and the weighting parameters in Eq. 4: $\beta^{Inner,BBMRI}$, $\beta^{Outer,BBMRI}$, $\beta^{Inner,EPIMRI}$, and $\beta^{Outer,EPIMRI}$. Since $\beta^{Inner,EPIMRI} = 1 - \beta^{Inner,BBMRI}$ and $\beta^{Outer,EPIMRI} = 1 - \beta^{Outer,BBMRI}$, we only need to optimize two weighting parameters: $\beta^{Inner,BBMRI}$ and $\beta^{Outer,BBMRI}$.

The average of the resulting best set of parameters for the three folds using each image sequence and combination are shown in Table I. In general, low parameter variation was observed, however, higher variations were observed in the parameters of the combination method. In BBMRI, a high variation was observed in p^{Inner}. We observed that the best wall separation penalty q is zero in all cases. This indicates that it is preferred not to penalize the distance between borders to allow segmentations of thick vessel walls in the presence of plaque. When combining several image sequences, the contribution of the BBMRI image information was larger than EPIMRI for detecting both the inner and outer wall. As EPIMRI is registered to BBMRI, small alignment errors may occur causing the lower contribution of EPIMRI image information. However, EPIMRI contributed more to detecting the outer wall, which could be explained by the high outer border contrast in the EPIMRI images. We observed higher values for p^{Outer} than for p^{Inner}. As in our MR images the inner border contrast is better than the outer border contrast, more smoothing of the segmentation is required for the outer border, while for the inner border it is possible to rely more

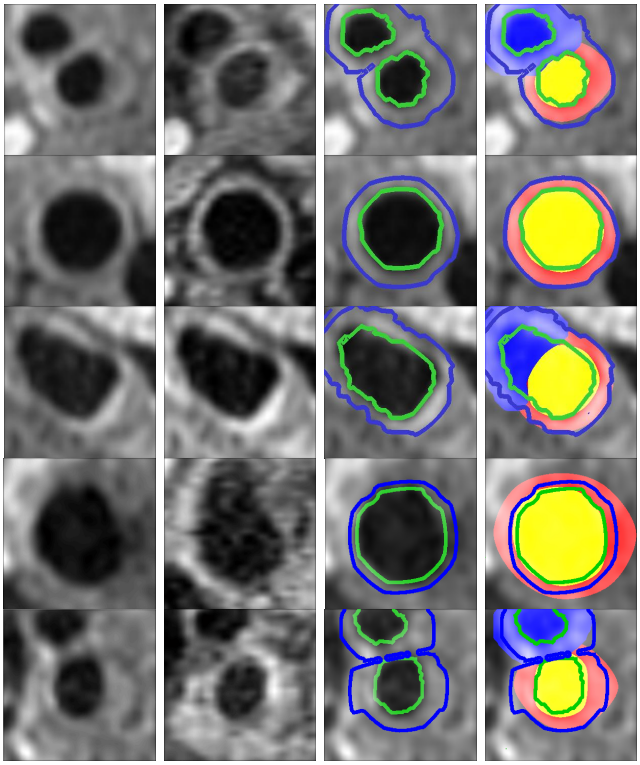

Fig. 4. Cross-sectional segmentation results using the proposed method combining BBMRI and EPIMRI image sequences. The BBMRI images are shown in the first column, and the EPIMRI image in the second column. The automatic segmentations are depicted by green (inner wall) and blue (outer wall) contours in the third column. The manual annotations are shown by the yellow surface (lumen) and the red surface (vessel wall) in the fourth column, with automatic segmentation results overlaid. The blue areas are excluded from evaluation, as the manual annotation described only part of the cross-section in the bifurcations.

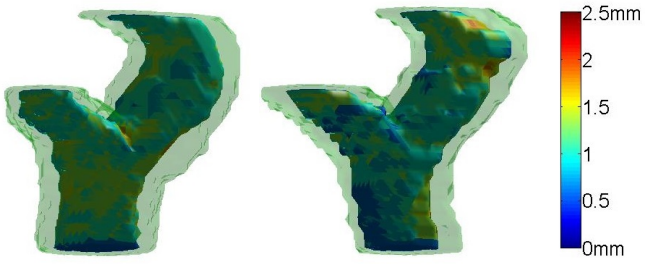

Fig. 5. Obtained 3D manual annotation (left) and automatic segmentation result (right) for the same carotid artery. The transparent green layer depicts the outer vessel border. The colors in the inner wall represent the wall thickness (mm).

on the local derivative information.

F. Comparison with manual annotations

Based on the best set of parameters determined in two of the folds, we applied the proposed segmentation method in the held out folds. Fig. 4 shows cross-sectional segmentation results using the proposed method combining BBMRI and EPIMRI. Further, Fig. 5 shows a 3D mask obtained from the manual annotations and the corresponding 3D segmentation result.

Table II shows the mean DSC between the automatic and manually annotated cross-sections from observer 1 for inner DSC^{Inner} and outer vessel borders DSC^{Outer} for the 57 carotid arteries. Additionally, the signed and absolute wall thickness differences (manual minus automatic) are shown in the table. To measure the wall thickness in the automatic and manual segmentations, we measured the mean distance between the inner border and the outer border over all points for each segmented cross-section. The distance for each point is measured along a ray from the centerline position and is given by the length of the segment stretching from inner border to outer border. We performed Friedman analysis and subsequently a post-hoc analysis based on Tukey-Kramer testing for multiple comparisons to determine which of the differences were significant. The highest average DSC for the inner border was obtained by combining BBMRI and EPIMRI image sequences, and this was significantly higher ($p = 0.01$) than for using only EPIMRI, but not significantly higher than for using only BBMRI. For the outer border the highest DSC was obtained using BBMRI only, which was significantly higher than using EPIMRI alone ($p = 0.04$). Thus, for both inner and outer wall segmentation no significant differences were observed between using both sequences and using only BBMRI. The mean wall thickness differences for the three options were very close, and no significant differences were observed. In all three cases a slight over-segmentation of the wall with respect to manual annotations of less than the voxel size was observed.

To evaluate how the method performs in the presence of disease represented as a wall thickening; we evaluated the inner and outer DSC of all manual and automatic cross-sections as a function of the wall thickness. The wall thickness per cross-section was measured as the 90% percentile distance between inner border points to the outer border (we do not use the maximum wall thickness as this is more sensitive to noise in the measures). The DSC for increasing wall thickness is shown in Fig. 6. From the figure we see that similar results were obtained for BBMRI and the combination of BBMRI and EPIMRI. For these two options the results are very robust to thickening of the wall, both for the inner and outer wall. In the remainder of this section, all results reported are for the method combining BBMRI and EPIMRI images.

TABLE II
DSC OVERLAP FOR INNER BORDER (DSC^{Inner}) AND OUTER BORDER (DSC^{Outer}), AND SIGNED AND ABSOLUTE WALL THICKNESS DIFFERENCES (SWTD, AWTD) BETWEEN THE AUTOMATIC AND MANUAL ANNOTATED CROSS-SECTIONS FOR EACH IMAGE SEQUENCE COMBINATION († SHOWS THAT THOSE RESULTS WERE SIGNIFICANTLY DIFFERENT TO EPIMRI).

	BBMRI	EPIMRI	BBMRI & EPIMRI
DSC^{Inner}	0.88 ± 0.06	0.88 ± 0.03	$0.89 \pm 0.05^{\dagger}$
DSC^{Outer}	$0.86 \pm 0.06^{\dagger}$	0.85 ± 0.05	0.85 ± 0.06
SWTD (mm)	-0.15 ± 0.3	-0.19 ± 0.4	-0.22 ± 0.4
AWTD (mm)	0.26 ± 0.2	0.34 ± 0.3	0.37 ± 0.2

Scatter plots of the volumes for automated segmentations against the manual annotations from observer 1, as measured in the upsampled cross-sectional slices, are given in Fig. 7

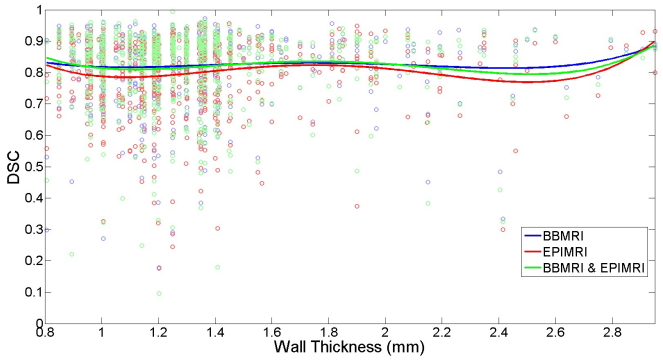

(a) DSC^{Inner}

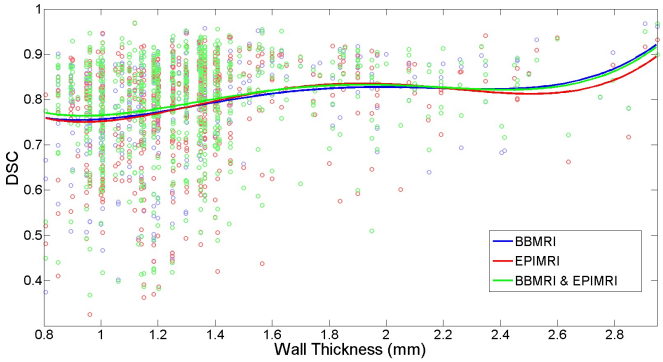

(b) DSC^{Outer}

Fig. 6. DSC as a function of maximum wall thickness for each image sequence and their combination, for all cross-sections. The wall thickness is represented by the 90% percentile thickness in the manually segmented cross-section. Finally, polynomial curves that fit the points for each of the sequence combinations are shown in the figures.

for lumen and vessel wall. We found an excellent correlation $ICC = 0.99$ between lumen volumes and a good correlation $ICC = 0.72$ between wall volumes.

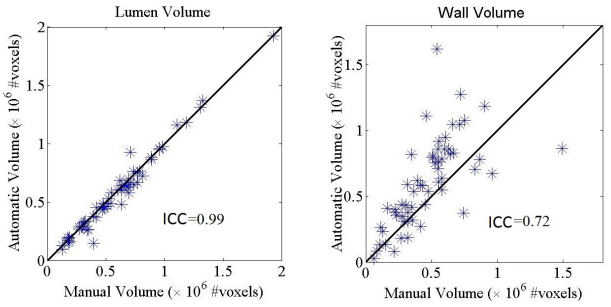

(a) (b)

Fig. 7. Scatter plots comparing manual and the automatic segmented lumen volumes (a), and wall volumes (complete vessel-lumen segmentation) (b) using the proposed segmentation method combining BBMRI and EPIMRI image sequences.

Finally, we compared the results of the proposed method to the manual segmentations from the second observer. As the second observer segmented only ICA and CCA, the ECA sections of the segmentations by the proposed method and by observer 1 were excluded. Using the manual ECA segmentations of observer 1, we created the exclusion area by creating a 3D mask of this manually annotated ECA section, and applied an axial dilation with a disk structuring element of 3mm radius to guarantee the exclusion of the automatically segmented ECA. Subsequently, we cropped the segmented volumes such that all segmentations were defined in all axial slices. Finally, we computed DSC outside the excluded area. The results for the subset of 28 carotid arteries that were manually annotated by both observers are described in Table III. The overlap of the automatic lumen segmentations and the segmentations of observer 1, was significantly higher ($p < 0.001$) than the overlap between observer 1 and observer 2, and the overlap between observer 2 and the automatic segmentations. For the outer border, the overlap between observer 1 and observer 2 was significantly higher than the overlap between observer 1 and the automatic segmentation, and between observer 2 and the automatic segmentation. From the SWTD results, we observed an over-segmentation of the wall with respect to observer 1 and an under-segmentation with respect to observer 2. Based on the AWTD, agreement of wall thickness measures was better between the automated approach and both observers than between observers.

G. Reproducibility analysis

Scan-rescan reproducibility was assessed on 30 patients who were imaged twice within a short time interval (15 ± 9 days). Significant changes in carotid anatomy were therefore not expected, and lumen and wall volume must be similar. The proposed method, combining BBMRI and EPIMRI images using the average set of parameters as described in Table II, was applied to the baseline and follow-up images of 60 carotid arteries. All segmented volumes were cropped from 13.5mm below up to 9mm above a manually allocated carotid bifurcation point in order to compare similar regions on baseline and follow-up. Scatter plots describing the correlations for lumen and vessel wall volumes between baseline and follow-up are shown in Figures 8(a) and 8(b). The obtained intraclass correlation for the lumen volumes is $ICC = 0.96$, and for the wall $ICC = 0.74$. The mean absolute wall volume difference between scan-rescan was $23\% \pm 23\%$. Figures 8(c) and 8(d) show an example of a baseline and follow-up segmentation pair.

H. Comparison with Other methods

Finally, we compared the proposed method to another carotid artery wall segmentation method in MRI on a public data set. Hameeteman et al. [12] proposed a cylindrical deformable surface model with a learning-based postprocessing step to segment the carotid artery wall in MRI. We choose this method because these results were made publicly available at http://ergocar.bigr.nl. In addition, to date their reported results are among the best for carotid artery wall segmentation in MRI. As only ICA and CCA were segmented using the method presented in [12] the segmented ECA sections were excluded from our resulting segmentations as described in section III-F. Subsequently, we cropped the segmented volumes 25mm centered at the bifurcation point as described in [12]. Fourteen subjects were used for the evaluation. From the 28 carotid arteries, one was discarded due to manual annotation errors

TABLE III
AGREEMENT BETWEEN THE AUTOMATIC METHOD, OBSERVER 1 (OBS. 1) AND OBSERVER 2 (OBS. 2). [1], [2] AND [3] INDICATE THAT THE OBTAINED RESULT IS SIGNIFICANTLY BETTER THAN THE CORRESPONDING RESULTS IN ROW 1, 2 OR 3, RESPECTIVELY. FOR THE AUTOMATIC SEGMENTATIONS, WE COMBINED BBMRI AND EPIMRI. THE ECA HAS BEEN EXCLUDED FOR THIS ANALYSIS, SO VALUES ARE DIFFERENT FROM TABLE II.

	DSC^{Inner}	DSC^{Outer}	SWTD (mm)	AWTD (mm)
Obs. 1 Vs. Obs. 2	0.81 ± 0.04	$0.91 \pm 0.04^{2,3}$	-0.62 ± 0.25	0.62 ± 0.25
Obs. 1 Vs. Auto	$0.88 \pm 0.06^{1,3}$	0.83 ± 0.06	-0.27 ± 0.4^{3}	0.41 ± 0.24^{1}
Obs. 2 Vs. Auto	0.78 ± 0.04	0.84 ± 0.08	0.34 ± 0.4	0.39 ± 0.4^{1}

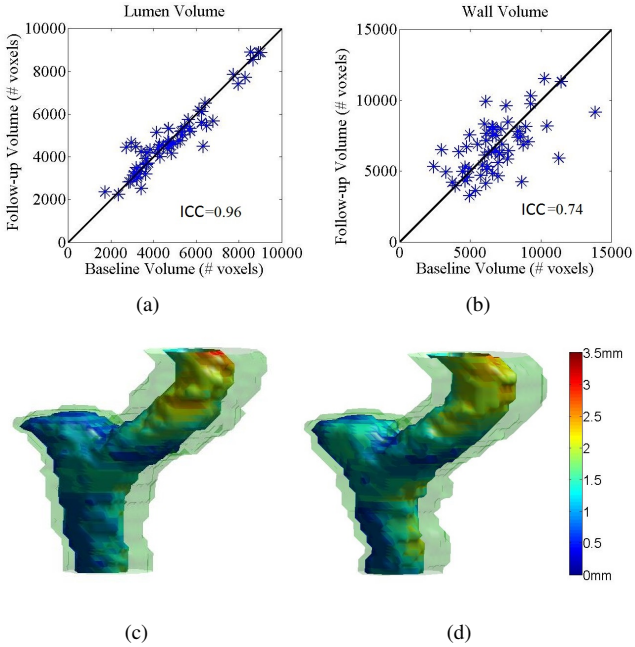

(a) (b) (c) (d)

Fig. 8. Comparison of baseline and short-term follow-up segmentations. (a) and (b) depict scatter plots comparing baseline and follow-up segmented lumen volumes (a), and wall volumes (b). The scatter plots show the results for 60 carotid arteries. In (c) a segmented baseline is shown, and (d) shows the corresponding segmented follow-up.

and four others because we observed big displacements on the ECA sections between automatic and manual segmentations and it was not possible to exclude the ECA using the method described in section III-F. Table IV shows the DSC on the manually annotated volumes from observer 1 for inner and outer border using both methods in 23 arteries. For the inner border, the presented method was significantly better ($p < 0.01$), while for the outer border it was not significantly different ($p = 0.06$). In addition, Table IV shows the SWTD and AWTD (manual-automatic) for both methods, here we observed lower SWTD and significantly lower AWTD using the method proposed by Hameeteman et al. [12] ($p < 0.01$).

IV. DISCUSSION

In this paper, we presented a new 3D method for carotid artery wall segmentation in MRI. This finds a globally optimal solution based on a cost function and jointly segments the complete lumen and outer wall including the bifurcation section. The method requires an initialization to build the graph. However, as the graph column trajectories extend both inwards

TABLE IV
COMPARISON OF THE PROPOSED METHOD TO THE METHOD PROPOSED BY HAMEETEMAN ET AL. [12] USING DSC FOR INNER (DSC^{Inner}) AND OUTER BORDER (DSC^{Outer}) BETWEEN AUTOMATIC RESULTS AND 3D MANUAL ANNOTATIONS, AND SIGNED AND ABSOLUTE WALL THICKNESS DIFFERENCES (SWTD, AWTD) BETWEEN AUTOMATIC AND MANUAL ANNOTATED CROSS-SECTIONS († SHOWS THAT THOSE RESULTS WERE SIGNIFICANTLY BETTER THAN THE OTHER METHOD).

	Hameeteman et al. [12]	Proposed Method
DSC^{Inner}	0.87 ± 0.09	$0.91 \pm 0.04^{\dagger}$
DSC^{Outer}	0.88 ± 0.08	0.86 ± 0.05
SWTD (mm)	-0.02 ± 0.24	-0.14 ± 0.54
AWTD (mm)	$0.20 \pm 0.15^{\dagger}$	0.46 ± 0.30

and outwards from this initialization, a coarse approximation of the lumen is sufficient.

We evaluated the quality of the automatic segmentations by cross-validation and comparison with manual segmentations performed by two experts. We also evaluated the method using several image combinations (BBMRI, EPIMRI, and BBMRI & EPIMRI). Based on the cross-validation, we did not observe big DSC variances using different parameter settings as shown in Table II. This means that the methods are able to generalize to unseen data acquired with a similar scan protocol. However, to apply the method to data acquired with a different scan protocol, the method parameters need to be re-tuned, as is the case for most segmentation approaches. The results for all combinations were good, with lumen overlap $DSC^{Inner} > 0.88$ and complete vessel overlap $DSC^{Outer} > 0.85$, and absolute wall thickness differences $AWTD < 0.37mm$, less than the in-plane voxel size. Segmentations based on EPIMRI had the lowest accuracy. This can be partly explained by the fact that the manual annotations were performed in BBMRI. Therefore possible misregistrations of EPIMRI to BBMRI are measured as segmentation errors in EPIMRI, and in cases where low image contrast or artefacts in BBMRI lead to a certain annotation, this is more likely to be reproduced by an automatic segmentation using BBMRI than by one using EPIMRI. Similar results with no significant differences were observed between BBMRI and the combination of BBMRI and EPIMRI. This similarity was also observed in the relation with wall thickness, where both methods had similar good performances in healthy and diseased sections of the artery. We conclude that the proposed edge cost function that can integrate information from several images will give better or similar results than using only one image. In cases where the available images only have good contrast in one of the borders

to segment, such combined cost function can be beneficial. However, as BBMRI itself has a good inner and a fair outer wall contrast, combining BBMRI with EPIMRI did not make a difference in our experiments.

The segmentation errors we obtained for the artery lumen are comparable to the inter-observer variation. As can be seen in Figure 3(a), Observer 2 showed a strong, consistent undersegmentation of the lumen with respect to Observer 1, which resulted in a relatively low agreement of this observer with both the automated method and Observer 1. This underlines the importance of objective measurements, such as those obtained automatically in this paper, in the analysis of carotid MR images. For the outer border, the overlap with the manual annotations of both observers was significantly lower than between observers. This lower accuracy at the outer border was also visible in the reproducibility study in the scatter plots in Figure 8(b) where the variation in wall volume measured in repeated scans is larger than the variation in lumen volume. Even though the correlation for the wall volumes is lower, we believe the proposed method presents a good reproducibility for lumen and wall volumes, as these correlations were higher compared to the inter-observer volume correlations. This is an important result: if we can measure similar volumes for the scan-rescan images, we should be able to do volume tracking for longitudinal analysis in clinical intervals. One possible reason for the lower performance at the outer border could be that the outer border contrast is often lower. The proposed cost function based on intensity image derivatives may therefore fail. In such cases, a cost function that integrates more features in addition to image intensity derivatives might give a better representation of the location of the outer border.

We compared the proposed method to the method presented in [12], which is an improved version of [9]. In [12], they reported statistically better results than those obtained using van 't Klooster et al. [9] ($DSC^{Inner} = 0.83$ and outer border $DSC^{Outer} = 0.85$). In this paper, the comparisons were performed on CCA and ICA only, because the method presented in [12] cannot segment the complete bifurcation. We obtained better DSC^{Inner} and the method presented in [12] resulted in lower wall thickness differences. Despite the similarity of the results, we consider our method relevant for this application as it can segment the complete bifurcation, which is medically relevant using a single graph cut segmentation. On the other hand, methods such as [12], which search a single tubular shape, could be used to segment the entire bifurcation by segmenting the individual vessel segments separately and joining the resulting segmentations. However, this may result in errors in the bifurcation region where the model of a single tube shape is not appropriate. Methods to segment only the lumen such as [6] reported a $DSC^{Inner} = 0.89$, which is similar to the reported DSC^{Inner} for the proposed method. Further, Ukwatta et al. [10] reported an average inner border $DSC^{Inner} > 0.85$ and outer border $DSC^{Outer} > 0.87$ using similar images. These results are comparable to the results obtained by our method, however, results cannot be compared directly as the data used for validation is different. Advantages of the proposed method are that it requires less user interaction than the method presented by Ukwatta et al. [10] therefore it is easier to fully automate using automated seed point detection or lumen detection methods as in [31], and that it can segment the complete bifurcation in one global optimization in contrast to Hameeteman et al. [12] and van 't Klooster et al. [9].

Because of the good quality inner border segmentations, the presented method can be used in clinical practice for lumen stenosis detection, or to analyze abnormalities in the carotid artery geometry. Additionally, the method can be used to analyze the vessel wall in large population studies. For wall analysis in clinical practice, an interactive approach that would allow more accurate quantitative wall measurements may be desirable.

V. Conclusion

To conclude, we have presented an optimal surface graph-based method for segmenting the complete carotid artery wall, which requires minimal user interaction and can combine information from several images. The method shows good agreement with manual segmentations. In contrast to previous approaches, our method jointly optimizes both surfaces: inner and outer border, finds a globally optimal solution, and can reliably segment the bifurcation section which is the most clinically relevant area to assess.

References

[1] Lozano et al., "Global and regional mortality from 235 causes of death for 20 age groups in 1990 and 2010: a systematic analysis for the global burden of disease study 2010," *The Lancet*, vol. 380, no. 9859, pp. 2095 – 2128, 2013.

[2] M. Sitzer, W. Muller, M. Siebler, W. Hort, H. W. Kniemeyer, L. Jancke, and H. Steinmetz, "Plaque ulceration and lumen thrombus are the main sources of cerebral microemboli in high-grade internal carotid artery stenosis," *Stroke*, vol. 26, no. 7, pp. 1231–1233, Jul 1995.

[3] R. Alizadeh Dehnavi, J. Doornbos, J. T. Tamsma, M. Stuber, H. Putter, R. J. van der Geest, H. J. Lamb, and A. de Roos, "Assessment of the carotid artery by MRI at 3T: A study on reproducibility," *Journal of Magnetic Resonance Imaging*, vol. 25, no. 5, pp. 1035–1043, 2007.

[4] N. Takaya, C. Yuan, B. Chu, T. Saam, H. Underhill, J. Cai, N. Tran, N. L. Polissar, C. Isaac, M. S. Ferguson, G. A. Garden, S. C. Cramer, K. R. Maravilla, B. Hashimoto, and T. S. Hatsukami, "Association between carotid plaque characteristics and subsequent ischemic cerebrovascular events: A prospective assessment with MRI—initial results," *Stroke*, vol. 37, no. 3, pp. 818–823, 2006.

[5] K. Hameeteman, M. Zuluaga, M. Freiman, L. Joskowicz, O. Cuisenaire, L. F. Valencia, M. Gulsun, K. Krissian, J. Mille, W. Wong, M. Orkisz, H. Tek, M. H. Hoyos, F. Benmansour, A. Chung, S. Rozie, M. van Gils, L. van den Borne, J. Sosna, P. Berman, N. Cohen, P. Douek, I. Sánchez, M. Aissat, M. Schaap, C. Metz, G. P. Krestin, A. van der Lugt, W. Niessen, and T. van Walsum, "Evaluation framework for carotid bifurcation lumen segmentation and stenosis grading," *Medical Image Analysis*, vol. 15, no. 4, pp. 477–488, 8 2011.

[6] H. Tang, T. van Walsum, R. S. van Onkelen, K. Hameeteman, S. Klein, M. Schaap, Q. J. B. Bouwhuijsen, J. Witteman, A. van der Lugt, L. J. van Vliet, and W. Niessen, "Semiautomatic carotid lumen segmentation for quantification of lumen geometry in multispectral MRI," *Medical Image Analysis*, vol. 16, no. 6, pp. 1202–1215, 8 2012.

[7] H. M. Ladak, J. S. Milner, and D. A. Steinman, "Rapid three-dimensional segmentation of the carotid bifurcation from serial MR images," *J Biomech Eng*, vol. 122, no. 1, pp. 96–99, Feb 2000.

[8] Y. Jin and H. M. Ladak, "Software for interactive segmentation of the carotid artery from 3D black blood magnetic resonance images," *Comput Methods Programs Biomed*, vol. 75, no. 1, pp. 31–43, Jul 2004.

[9] R. van 't Klooster, P. J. de Koning, R. A. Dehnavi, J. T. Tamsma, A. de Roos, J. H. Reiber, and R. J. van der Geest, "Automatic lumen and outer wall segmentation of the carotid artery using deformable three-dimensional models in MR angiography and vessel wall images," *Journal of Magnetic Resonance Imaging*, vol. 35, no. 1, pp. 156–165, 2012.

[10] E. Ukwatta, J. Yuan, M. Rajchl, W. Qiu, D. Tessier, and A. Fenster, "3-D carotid multi-region MRI segmentation by globally optimal evolution of coupled surfaces," *Medical Imaging, IEEE Transactions on*, vol. 32, no. 4, pp. 770–785, 2013.

[11] A. Arias, J. Petersen, A. van Engelen, H. Tang, M. Selwaness, J. Witteman, A. Lugt, W. Niessen, and M. Bruijne, "Carotid artery wall segmentation by coupled surface graph cuts," in *Medical Computer Vision. Recognition Techniques and Applications in Medical Imaging*, ser. Lecture Notes in Computer Science. Springer Berlin Heidelberg, 2013, vol. 7766, pp. 38–47.

[12] K. Hameeteman, R. van 't Klooster, M. Selwaness, A. van der Lugt, J. Witteman, W. Niessen, and S. Klein, "Carotid wall volume quantification from magnetic resonance images using deformable model fitting and learning-based correction of systematic errors," *Physics in Medicine and Biology*, vol. 58, 2013.

[13] M. Freiman, N. Broide, M. Natanzon, E. Nammer, O. Shilon, L. Weizman, L. Joskowicz, and J. Sosna, "Vessels-cut: a graph based approach to patient-specific carotid arteries modeling," in *Proceedings of the 2009 international conference on Modelling the Physiological Human*, ser. 3DPH'09. Berlin, Heidelberg: Springer-Verlag, 2009, pp. 1–12.

[14] C. Bauer, T. Pock, E. Sorantin, H. Bischof, and R. Beichel, "Segmentation of interwoven 3d tubular tree structures utilizing shape priors and graph cuts," *Medical Image Analysis*, Nov. 2009.

[15] X. Xu, M. Niemeijer, Q. Song, M. Garvin, J. Reinhardt, and M. Abramoff, "Retinal vessel width measurements based on a graph-theoretic method," in *Biomedical Imaging: From Nano to Macro, 2011 IEEE International Symposium on*, April 2011, pp. 641–644.

[16] A. Lorza, D. Carvalho, J. Petersen, A. Dijk, A. Lugt, W. Niessen, S. Klein, and M. Bruijne, "Carotid artery lumen segmentation in 3D free-hand ultrasound images using surface graph cuts," in *Medical Image Computing and Computer-Assisted Intervention – MICCAI 2013*, ser. Lecture Notes in Computer Science. Springer Berlin Heidelberg, 2013, vol. 8150, pp. 542–549.

[17] K. Li, X. Wu, D. Z. Chen, and M. Sonka, "Optimal surface segmentation in volumetric images – a graph-theoretic approach," *IEEE Transactions on Pattern Analysis and Machine Intelligence*, vol. 28, no. 1, pp. 119–134, 2006.

[18] J. Petersen, M. Nielsen, P. Lo, L. Nordenmark, J. Pedersen, M. Wille, A. Dirksen, and M. de Bruijne, "Optimal surface segmentation using flow lines to quantify airway abnormalities in chronic obstructive pulmonary disease," *Medical Image Analysis*, vol. 18, no. 3, pp. 531–541, 2014.

[19] X. Liu, D. Z. Chen, M. H. Tawhai, X. Wu, E. A. Hoffman, and M. Sonka, "Optimal graph search based segmentation of airway tree double surfaces across bifurcations," *IEEE Trans. Med. Imaging*, vol. 32, no. 3, pp. 493–510, 2013.

[20] M. A. Gülsün and H. Tek, "Robust vessel tree modeling," in *MICCAI*, ser. MICCAI '08. Berlin, Heidelberg: Springer-Verlag, 2008, pp. 602–611.

[21] H. Ishikawa, "Exact optimization for markov random fields with convex priors," *Pattern Analysis and Machine Intelligence, IEEE Transactions on*, vol. 25, no. 10, pp. 1333–1336, 2003.

[22] Y. Boykov and V. Kolmogorov, "An experimental comparison of min-cut/max-flow algorithms for energy minimization in vision," *IEEE Transactions on Pattern Analysis and Machine Intelligence*, vol. 26, no. 9, pp. 1124–1137, 2004.

[23] Q. J. van den Bouwhuijsen, M. W. Vernooij, A. Hofman, G. P. Krestin, A. van der Lugt, and J. C. Witteman, "Determinants of magnetic resonance imaging detected carotid plaque components: the rotterdam study," *European Heart Journal*, 2011.

[24] M. H. Rodallec, V. Marteau, S. Gerber, L. Desmottes, and M. Zins, "Craniocervical arterial dissection: Spectrum of imaging findings and differential diagnosis1," *Radiographics*, vol. 28, no. 6, pp. 1711–1728, 2008.

[25] G. Turk and J. F. O'Brien, "Shape transformation using variational implicit functions," in *Proceedings of the 26th annual conference on Computer graphics and interactive techniques*, ser. SIGGRAPH '99. ACM Press/Addison-Wesley Publishing Co., 1999, pp. 335–342.

[26] N. Tustison, B. Avants, P. Cook, Y. Zheng, A. Egan, P. Yushkevich, and J. Gee, "N4ITK: Improved N3 bias correction," *IEEE Transactions on Medical Imaging*, vol. 29(6), pp. 1310 – 1320, 2010.

[27] J. Krejza, M. Arkuszewski, S. E. Kasner, J. Weigele, A. Ustymowicz, R. W. Hurst, B. L. Cucchiara, and S. R. Messe, "Carotid artery diameter in men and women and the relation to body and neck size," *Stroke*, vol. 37, no. 4, pp. 1103–1105, 2006.

[28] R. van 't Klooster, M. Staring, S. Klein, R. Kwee, M. Kooi, J. H. C. Reiber, B. Lelieveldt, and R. van der Geest, "Automated registration of multispectral MR vessel wall images of the carotid artery," *Medical Physics*, vol. 40, no. 12, pp. 121 904–1 – 121 904–12, 2013.

[29] L. R. Dice, "Measures of the amount of ecologic association between species," *Ecology*, vol. 26(3), pp. 297–302, 1945.

[30] M. Silvestrini, B. Rizzato, F. Placidi, R. Baruffaldi, A. Bianconi, and M. Diomedi, "Carotid artery wall thickness in patients with obstructive sleep apnea syndrome," *Stroke*, vol. 33, no. 7, pp. 1782–1785, 2002.

[31] S. Liu, D. Padfield, and P. Mendonca, "Tracking of carotid arteries in ultrasound images," in *Medical Image Computing and Computer-Assisted Intervention – MICCAI 2013*, ser. Lecture Notes in Computer Science. Springer Berlin Heidelberg, 2013, vol. 8150, pp. 526–533.